

# Three-dimensional numerical simulation of the velocity fields induced by submerged breakwaters

G. Cannata, F. Gallerano, F. Palleschi, C. Petrelli, and L. Barsi

**Abstract**— We propose a three-dimensional numerical model for non-hydrostatic free surface flows in which the Navier-Stokes equations are expressed in integral form on a coordinate system in which the vertical coordinate is varying in time. By a time-dependent coordinate transformation, the irregular time varying physical domain is transformed into a uniform fixed computational domain, in which the equations of motion are numerically integrated by a shock-capturing scheme based on WENO reconstruction and an approximate HLL Riemann Solver. The proposed model is used to simulate free surface elevation and three-dimensional velocity fields induced by normally incident waves on a beach with submerged breakwaters. The three-dimensional numerical results are compared with experimental measurements and with the numerical results obtained by a depth-averaged horizontal two-dimensional model. This comparison shows that features of three-dimensionality in the fluid flow induced by wave-structure interaction, as the undertow, can be correctly simulated by the proposed non-hydrostatic three-dimensional model.

**Keywords**—Three-dimensional, time-dependent coordinates, free-surface flow, undertow

## I. INTRODUCTION

**I**N recent years, fluid-structure interaction has been the subject of numerous research activities, that range from experimentally simulating the flow of blood in arteries [1], or the airflow between urban buildings [2]-[3] to numerically simulating the airflow around a bridge deck [4]-[5].

In the present paper we present a numerical study on the fluid-structure interaction between sea's waves and submerged breakwaters.

Submerged breakwaters for coastal defence are a good

G. Cannata is with the Department of Civil, Constructional and Environmental Engineering, "Sapienza" University of Rome, Via Eudossiana, 18, 00184 Rome, Italy (corresponding author to provide phone: +39 0644585062; e-mail: giovanni.cannata@uniroma1.it).

F. Gallerano is with the Department of Civil, Constructional and Environmental Engineering, "Sapienza" University of Rome, Via Eudossiana, 18, 00184 Rome, Italy (e-mail: francesco.gallerano@uniroma1.it).

F. Palleschi is with the Department of Civil, Constructional and Environmental Engineering, "Sapienza" University of Rome, Via Eudossiana, 18, 00184 Rome, Italy (e-mail: federica.palleschi@uniroma1.it).

C. Petrelli is with the Department of Civil, Constructional and Environmental Engineering, "Sapienza" University of Rome, Via Eudossiana, 18, 00184 Rome, Italy (e-mail: chiara.petrelli@uniroma1.it).

L. Barsi is with the Department of Civil, Constructional and Environmental Engineering, "Sapienza" University of Rome, Via Eudossiana, 18, 00184 Rome, Italy (e-mail: luca.barsi@uniroma1.it).

compromise between the need to mitigate the effects of waves on the coast and the ambition to ensure the preservation of the landscape and water quality. The main function of this structure is to protect the shoreward area of the breakwater from wave actions by way of attenuating the incoming waves. Submerged breakwaters lower the wave energy in the protected area by provoking the breaking of the incoming waves over the structure.

However, if not properly designed, such structures can force circulation patterns that enhance shoreline erosion rather than shoreline accretion.

In fact, the presence of submerged breakwaters can produce alongshore gradients in surface elevation between the landward side of submerged breakwaters and the gaps. Such gradients drive longshore flows away from the structure in both longshore

directions, which return offshore through the gaps for continuity requirements (Primary Circulation System). This circulation system can induce shoreline erosion. The extent of the primary circulation system could be limited by a further current closer to the shoreline, opposed in sign to the former. This is the case in which the wave set-up at the shoreline due to the breaking of waves entering the sheltered area through the gaps is larger than the wave setup caused by re-shoaling and breaking of the transmitted waves over the breakwaters and a secondary circulation system takes place.

According to the simple response-function model proposed by Ranasinghe et al. [6], erosion at the shoreline is expected to occur when the resultant current field contains divergent alongshore currents in the entire protected zone return offshore again at the gaps transporting sediments out of the protected area (circulation of an erosive nature). Accretion at the shoreline is expected when an additional converging flow closer to the shoreline, promoting sediment deposition, is generated (circulation of an accretive nature).

The need to fully understand the hydraulic behaviour of submerged breakwaters has triggered a large amount of research into this topic.

Coastal currents and, more generally, hydrodynamic phenomena produced by wave-structure interaction have features of three-dimensionality that are locally important [7]. The most important of the above three-dimensional phenomena and the cause of offshore sediment transport is the

undertow [8] which consists of a circulation in the vertical plane in which the near-bed current velocities are off-shore directed in the surf zone [9].

Numerical models can be used to investigate the structure-induced circulation patterns and the resulting sediment transport response.

In literature, the current circulations are generally simulated by two-dimensional Boussinesq models [10]-[11]-[12]-[13] obtained by depth-averaging a simplified form of the three-dimensional Navier-Stokes equations. This approach, based on the depth-averaged motion equations, assumes a simplified distribution of the hydrodynamic quantities along the vertical direction and proves to be valid only in the cases in which a fully three-dimensional representation of the fluid flow is not needed.

A different approach that takes into account the three-dimensional aspects of motion, as the undertow current, is based on the numerical integration of the non-hydrostatic Navier-Stokes equations by taking into account the dynamic pressure [14]. Using this approach, the total pressure is split into its dynamic part and hydrostatic part.

In this work, we propose a three-dimensional numerical model in which the non-hydrostatic Navier-Stokes equations are expressed in integral form on a coordinate system in which the vertical coordinate is varying in time. The boundary conditions for pressure are placed on the upper face of each computational cell. The solution is advanced in time by using a three-stage Strong Stability Preserving Runge-Kutta (SSPRK) fractional step numerical method, and at each stage a pressure correction formulation is applied in order to get a fluid velocity field which is divergence-free. A shock-capturing technique based on high-order WENO reconstructions is employed in order to discretize the fluid motion equations. At every cell interface, the numerical flux is computed by solving an approximate HLL Riemann problem.

The proposed model is used to simulate the circulation patterns induced by normally incident waves on a beach with submerged longshore bars and rip channels [15]-[16]. The numerical results are compared with experimental measurements and with the numerical results obtained by a depth-averaged two-dimensional model [11]. The results obtained show that features of three-dimensionality in the fluid flow induced by wave-structure interaction are locally important and entails the need of a fully three-dimensional model.

## II. THE PROPOSED MODEL

### A. Governing integral three-dimensional $\sigma$ -coordinate equations

The integral form of the momentum equations over a control volume  $\Delta V(t)$  which varies in time is given by

$$\begin{aligned} & \frac{d}{dt} \int_{\Delta V(t)} \rho u_i dV + \int_{\Delta A(t)} \rho u_i (u_m - v_m) n_m dA \\ & = \int_{\Delta V(t)} \rho f_i dV + \int_{\Delta A(t)} T_{lm} n_m dA \end{aligned} \quad (1)$$

where  $\Delta A(t)$  is the surface of the control volume,  $n_m$  ( $m = 1,3$ ) is the outward unit normal vector to the surface  $\Delta A(t)$ ,  $u_i$  ( $i = 1,3$ ) and  $v_m$  ( $m = 1,3$ ) are respectively the fluid velocity and the velocity of the surface of the control volume, both defined in a Cartesian reference system of coordinates  $x^l$  ( $l = 1,3$ ),  $\rho$  is the density of the fluid,  $T_{lm}$  is the stress tensor and  $f_i$  ( $i = 1,3$ ) represents the external body forces per unit mass vector

$$f_i = -\frac{1}{\rho} p_{,i} - G \delta_{i3} \quad (2)$$

in which  $\delta_{13}$  is the Kroneker symbol and  $p$  is the total pressure defined by the sum of the hydrostatic and the dynamic component

$$p = \rho G (\eta - x^3) + q \quad (3)$$

where  $G$  is the constant of gravity,  $q$  is the dynamic pressure,  $\eta$  is the free surface elevation, the comma with an index in subscript denotes the derivative as  $[ \ ]_{,i} = \partial [ \ ] / \partial x^i$  and  $(x^1, x^2, x^3, t)$  is a Cartesian coordinate system. The first integral on the right-hand side of equation (1) can be rewritten as

$$\int_{\Delta V(t)} \rho f_i dV = - \int_{\Delta V(t)} [(\rho G \eta + q)_{,i}] dV \quad (4)$$

By applying Green's theorem, the right-hand side (4) becomes

$$\begin{aligned} & - \int_{\Delta V(t)} [(\rho G \eta + q)_{,i}] dV = \\ & - \int_{\Delta A(t)} \rho G \eta n_i dA - \int_{\Delta V(t)} [q]_{,i} dV \end{aligned} \quad (5)$$

By introducing equation (5) in equation (1)

$$\begin{aligned} & \frac{d}{dt} \int_{\Delta V(t)} \rho u_i dV = \\ & - \int_{\Delta A(t)} [\rho u_i (u_m - v_m) n_m + \rho G \eta n_i] dA \\ & - \int_{\Delta V(t)} [q]_{,i} dV + \int_{\Delta A(t)} T_{lm} n_m dA \end{aligned} \quad (6)$$

In order to simulate the fully dispersive wave processes, (6) can be transformed in the following way.

Let  $H(x^1, x^2, t) = h(x^1, x^2, t) + \eta(x^1, x^2, t)$  where  $h$  is the depth of still water. Let  $(\xi^1, \xi^2, \xi^3, \tau)$  be a system of curvilinear coordinates which varies in time so as to follow the time variation of the free-surface elevation, the transformation from the Cartesian coordinates  $(x^1, x^2, x^3, t)$  to the curvilinear coordinates is

$$\xi^1 = x^1, \quad \xi^2 = x^2, \quad \xi^3 = \frac{x^3+h}{H}, \quad \tau = t \quad (7)$$

The following relation is valid

$$v_3 = \frac{\partial x^3}{\partial \tau} \quad (8)$$

This coordinate transformation basically maps the varying vertical coordinates in the physical domain to a uniform transformed space where  $\xi^3$  spans from 0 to 1.

By following the procedure proposed by [8] we define the transformation matrix  $C_m^l = \partial x^l / \partial \xi^m$  and its inverse  $\bar{C}_m^l = \partial \xi^l / \partial x^m$  ( $l, m = 1, 3$ ). The metric tensor and its inverse are defined by  $g_{lm} = C_l^k C_m^k$  and  $g^{lm} = \bar{C}_l^k \bar{C}_m^k$ , respectively. The Jacobian of the transformation is defined by  $\sqrt{g} = \det(C_m^l)$ . It is not difficult to verify that in the above-mentioned transformation  $\sqrt{g} = H$ .

In the following  $\Delta V(t)$  must be considered as a volume element defined by surface elements bounded by curves lying on the coordinate lines. Consequently, we define the volume element  $\Delta V(t) = \Delta x^1 \Delta x^2 \Delta x^3 = \sqrt{g} \Delta \xi^1 \Delta \xi^2 \Delta \xi^3$  in the physical space, and the volume element in the transformed space  $\Delta V^* = \Delta \xi^1 \Delta \xi^2 \Delta \xi^3$ . It is possible to see that the first volume element is time dependent while the second one is not.

In the same way we define the surface element in the physical space  $\Delta A(t) = \Delta x^\alpha \Delta x^\beta = \sqrt{g} \Delta \xi^\alpha \Delta \xi^\beta$  and the surface element in the transformed space  $\Delta A^* = \Delta \xi^\alpha \Delta \xi^\beta$  (in which  $\alpha, \beta = 1, 2, 3$  are cyclic). We define the averaged cell value (in the transformed space) of primitive variables

$$\bar{H} = \frac{1}{\Delta V^*} \int_{\Delta V^*} H d\xi^1 d\xi^2 d\xi^3 \quad (9)$$

$$\bar{u}_i = \frac{1}{\Delta V^*} \int_{\Delta V^*} u_i d\xi^1 d\xi^2 d\xi^3$$

and conserved variable

$$\overline{Hu}_i = \frac{1}{\Delta V^*} \int_{\Delta V^*} Hu_i d\xi^1 d\xi^2 d\xi^3 \quad (10)$$

The expression of the momentum equation reads

$$\begin{aligned} \frac{\partial \overline{Hu}_i}{\partial \tau} = \frac{1}{\Delta V^*} \{ & \sum_{\alpha=1}^3 \left\{ \int_{\Delta A^{*\alpha+}} [Hu_i(u_m - v_m) \bar{C}_m^\alpha + GH^2 \bar{C}_l^\alpha] d\xi^\beta d\xi^\gamma \right. \\ & \left. - \int_{\Delta A^{*\alpha-}} [Hu_i(u_m - v_m) \bar{C}_m^\alpha + GH^2 \bar{C}_l^\alpha] d\xi^\beta d\xi^\gamma \right\} + \\ & \sum_{\alpha=1}^3 \left( \int_{\Delta A^{*\alpha+}} GhH \bar{C}_l^\alpha d\xi^\beta d\xi^\gamma - \int_{\Delta A^{*\alpha-}} GhH \bar{C}_l^\alpha d\xi^\beta d\xi^\gamma \right) \\ & - \frac{1}{\rho} \int_{\Delta V^*} \frac{\partial q}{\partial \xi^k} \bar{C}_l^k H d\xi^1 d\xi^2 d\xi^3 + \end{aligned}$$

$$\sum_{\alpha=1}^3 \frac{1}{\rho} \left( \int_{\Delta A^{*\alpha+}} T_{lm} \bar{C}_m^\alpha H d\xi^\beta d\xi^\gamma + \int_{\Delta A^{*\alpha-}} T_{lm} \bar{C}_m^\alpha H d\xi^1 d\xi^\beta d\xi^\gamma \right) \quad (11)$$

where  $\Delta A^{*\alpha+}$  and  $\Delta A^{*\alpha-}$  indicate the contour surfaces of the volume element  $\Delta V^*$  on which  $\xi^\alpha$  is constant and which are located at the larger and at the smaller value of  $\xi^\alpha$  respectively. Here the indexes  $\alpha, \beta$  and  $\gamma$  are cyclic.

The total time derivative on the left-hand side of (11) is a local time derivative because the integral is a simple function of  $(\xi^1, \xi^2, \xi^3, \tau)$ . It is possible to see that the advancing in time of the conserved variables is applied in the transformed space that is not time varying. The time varying of the geometric components is expressed by the metric terms.

In order to ensure conservation of mass over the water column, we define a time-varying control volume,  $\Delta \tilde{V} = \Delta A_{xy}^* H$  where  $\Delta A_{xy}^* = \Delta \xi^1 \Delta \xi^2$ , and derive the following integral form of the continuity equation

$$\begin{aligned} \frac{\partial \bar{H}}{\partial \tau} + \frac{1}{\Delta A_{xy}^*} \int_0^1 \sum_{\alpha=1}^2 \left( \int_{\xi^{\alpha+}} Hu_\alpha d\xi^\beta - \int_{\xi^{\alpha-}} Hu_\alpha d\xi^\beta \right) d\xi^3 = 0 \quad (12) \end{aligned}$$

in which  $\xi^{\alpha+}$  and  $\xi^{\alpha-}$  indicate the contour lines of the surface element  $\Delta A^*$  on which  $\xi^\alpha$  is constant and which are located at the larger and at the smaller value of  $\xi^\alpha$  respectively. Equation (12) represents the governing equation for the surface movements.

Equations (11) and (12) represent the expressions of the three-dimensional motion equations as a function of the  $\overline{Hu}_i$  and  $\bar{H}$  variables in the time dependent coordinate system  $(\xi^1, \xi^2, \xi^3, \tau)$ . The numerical integration of the mentioned (11) and (12) allows the fully dispersive wave processes simulation.

The turbulent kinematic viscosity in the stress tensor is estimated by a Smagorinsky sub grid model.

### B. The Numerical Scheme

A combined finite-volume and finite-difference scheme with a Godunov-type method has been applied to discretize (11) and (12). By following the strategy described by [7]-[14] a staggered grid framework is introduced, in which the velocities are placed at the cell centres and the pressure is defined at the horizontal cell faces. The state of the system is known at the centre of the calculation cells and it is defined by the cell-averaged values  $\overline{Hu}_i$  and  $\bar{H}$ .  $\tau^{(n)}$  is the time level of the known variables while  $\tau^{(n+1)}$  is the time level of the unknown variables. The solution procedure uses a three-stage third-order nonlinear strong stability-preserving (SSP) Runge-Kutta scheme for (11) and (12). A pressure correction formulation is applied to obtain a divergence free velocity field at each time level. With  $\overline{Hu}_i^{(n)}$  known,  $\overline{Hu}_i^{(n+1)}$  is

calculated with the following three stage iteration procedure. Let

$$\overline{Hu}_l^{(0)} = \overline{Hu}_l^{(n)} \quad (13)$$

At each stage  $p$  (where  $p = 1, 2, 3$ ) an auxiliary field  $\overline{Hu}_{l*}^{(p)}$  are obtained directly from (11) by using values from the previous stage

$$\overline{Hu}_{l*}^{(p)} = \sum_{q=0}^{p-1} \{\Omega_{pq} \overline{Hu}_l^{(q)} + \Delta\tau \varphi_{pq} D[\overline{Hu}_l^{(q)}, \tau^{(n)} + d_q \Delta\tau]\} \quad (14)$$

where  $D(H, u_l, \tau)$  indicates the right-hand side of (11), in which the term related to the dynamic pressure gradient is omitted. See [1417] for the values of coefficients  $\Omega_{pq}$ ,  $\varphi_{pq}$  and  $d_q$ . The auxiliary velocity field  $\overline{u}_{l*}^{(p)}$  (associated with the auxiliary variable  $\overline{Hu}_{l*}^{(p)}$  calculated by (14) by using  $\overline{H}^{(p-1)}$ ) does not satisfy the continuity equation. In order to obtain a non-hydrostatic divergence-free velocity fields, the pressure field and the auxiliary velocity field are corrected, at each intermediate step  $p$ , by introducing a scalar potential  $\Psi$  which is calculated by the well-known Poisson pressure equation given by

$$\nabla^2 \Psi^{(p)} = -\frac{\rho}{\Delta t} \nabla(\overline{u}_{l*}^{(p)}) \quad (15)$$

Equation (15), expressed in the time dependent coordinate system, is given by

$$\begin{aligned} & \frac{\partial \partial \Psi^{(p)}}{\partial \xi^1 \partial \xi^1} + \frac{\partial \partial \Psi^{(p)}}{\partial \xi^2 \partial \xi^2} \\ & + \left[ \left( \frac{\partial \xi^3}{\partial x} \right)^2 + \left( \frac{\partial \xi^3}{\partial y} \right)^2 + \left( \frac{\partial \xi^3}{\partial z} \right)^2 \right] \frac{\partial \partial \Psi^{(p)}}{\partial \xi^3 \partial \xi^3} \\ & + 2 \left( \frac{\partial \xi^3}{\partial x} \frac{\partial \partial \Psi^{(p)}}{\partial \xi^1 \partial \xi^3} + \frac{\partial \xi^3}{\partial y} \frac{\partial \partial \Psi^{(p)}}{\partial \xi^2 \partial \xi^3} \right) + \left( \frac{\partial \partial \xi^3}{\partial x \partial \xi^1} + \frac{\partial \partial \xi^3}{\partial y \partial \xi^2} \right) \frac{\partial \Psi^{(p)}}{\partial \xi^3} = \\ & -\frac{\rho}{\Delta t} \left( \frac{\partial \overline{u}_{l*}^{(p)}}{\partial \xi^1} + \frac{\partial \overline{u}_{l*}^{(p)}}{\partial \xi^3} \frac{\partial \xi^3}{\partial x} + \frac{\partial \overline{u}_{l*}^{(p)}}{\partial \xi^2} + \frac{\partial \overline{u}_{l*}^{(p)}}{\partial \xi^3} \frac{\partial \xi^3}{\partial y} + \frac{\partial \overline{u}_{l*}^{(p)}}{\partial \xi^3} \frac{\partial \xi^3}{\partial z} \right) \end{aligned} \quad (16)$$

Equation (16) is defined at the horizontal cell centre and it is discretized by a second order cell centred finite-difference scheme. By this way (16) can be reduced to an algebraic linear system like  $A\Psi = b$ , where  $A$  is the coefficient matrix (with 15 non-zero diagonal coefficient),  $\Psi$  is the scalar potential vector and  $b$  is the vector of constant terms.

This algebraic linear system is solved by using an implicit scheme based on a four-colour Zebra line Gauss-Seidel alternate method [18] and a multigrid V-cycle accelerator as described in [19].

The implemented parallelization strategy is coherent with the adopted numerical scheme.

The Poisson equation solution technique needs an iterative procedure which can alternate the integrating directions within the three main coordinates. For these reasons, the computational domain is split into strips which follow the main direction along which the Poisson equation is integrated. By using the parallel computing system (MPI) the splitting of the computational domain is changed throughout the iterative procedure to follow the direction along which the numerical integration is performed.

The corrector irrotational velocity field is calculated by the following expressions

$$\overline{u}_{1c}^{(p)} = \frac{\Delta t}{\rho} \left( \frac{\partial \Psi^{(p)}}{\partial \xi^1} + \frac{\partial \Psi^{(p)}}{\partial \xi^3} \frac{\partial \xi^3}{\partial x} \right) \quad (17)$$

$$\overline{u}_{2c}^{(p)} = \frac{\Delta t}{\rho} \left( \frac{\partial \Psi^{(p)}}{\partial \xi^2} + \frac{\partial \Psi^{(p)}}{\partial \xi^3} \frac{\partial \xi^3}{\partial y} \right) \quad (18)$$

$$\overline{u}_{3c}^{(p)} = \frac{\Delta t}{\rho} \left( \frac{\partial \Psi^{(p)}}{\partial \xi^3} \frac{\partial \xi^3}{\partial z} \right) \quad (19)$$

To obtain a divergence-free velocity field at each stage and a non-hydrostatic velocity field, the velocity field must be corrected as

$$\overline{u}_l^{(p)} = \overline{u}_{l*}^{(p)} + \overline{u}_{lc}^{(p)} \quad (20)$$

Let us indicate with  $L(H, u_l, \tau)$  the right-hand side of (12). The advancing at the  $p$  stage of the depth  $\overline{H}^{(p)}$  is obtained by

$$\begin{aligned} \overline{H}^{(p)} &= \overline{H}^{(p-1)} + \\ L(\overline{H}^{(p-1)}, u_l^{(p-1)}, \tau^n + \Delta\tau) \end{aligned} \quad (22)$$

The value of  $\overline{Hu}_l^{(n+1)}$  is given by

$$\overline{Hu}_l^{(n+1)} = \overline{Hu}_l^{(3)} \quad (23)$$

The updating of the flow variables  $\overline{Hu}_l$  and  $\overline{H}$  is based on the following sequence.

(1) High order WENO reconstructions, from cell averaged values, of the point values of the unknown variables at the centre of the contour faces which define the calculation cells. At the centre of the contour face which is common with two adjacent cells, two-point values of the unknown variables are reconstructed by means of two WENO reconstruction defined on two adjacent cells [20]-[21].

(2) Advancing in time of the point values of the unknown variables at the centre of the contour faces by solving, by an HLL Riemann solver [22], a local Riemann problem with initial data given by the pair of point-values computed by two

WENO reconstructions defined on the two adjacent cells.

(3) Calculation of the spatial integrals on the right-hand side of (11) and (12).

(4) Solution of the Poisson pressure equation by using a four-color Zebra line Gauss-Seidel alternate method and a multigrid V-cycle.

(5) Correction of the hydrostatic velocity field by using a scalar potential  $\Psi$ .

(6) Advancing in time of the total local depth (12) by using the non-hydrostatic velocity field.

### III. THREE-DIMENSIONAL NEARSHORE CURRENTS INDUCED BY SUBMERGED BREAKWATERS

The model is used to simulate the circulation patterns induced by normally incident waves on a beach with a longshore bar and rip channels. The experimental test performed by [15] on a fixed barred beach with periodically spaced rip channels is here reproduced by the presented three-dimensional non-hydrostatic model.

The model is also validated against the laboratory measurement of [9] and a two-dimensional numerical model for free-surface flows [11], based on the Boussinesq equations, that has been successfully verified for a range of experimental data. In the validations, we focus on the circulation patterns enhanced by the presence of submerged breakwaters – that produce the erosion or accretion of the shoreline – and the undertow.

#### A. Governing integral three-dimensional $\sigma$ -coordinate equations

A deep insight about the different circulation patterns that can arise in presence of submerged breakwaters and normally incident waves can be found in [6] and in [16]. They presented a relationship linking environmental and geometrical properties of the system to the shoreline mode of response, i.e. accretive or erosive, thus identifying two different types of structure-induced circulation current.

Because of the presence of the submerged breakwaters, the incoming waves break at different abscissa along the shoreline: the incoming waves directly approaching the shore through the gaps steepen and finally break due to water depth limitations; whilst the reduction of wave energy due to the wave breaking over the structure causes the transmitted waves to break closer to the shoreline than those at the gaps and with a smaller wave set-up.

These set-up variations govern the flow patterns in the protected area behind the structures.

Mass conservation requires that the water flowing onshore over the barrier returns off-shore again through the gaps. The resulting diverging current circulation system in the lee of the breakwater is composed of two symmetric circulation cells and drive sediments out of the protected area causing shoreline erosion (Fig. 1). Nevertheless, depending on the direction of the alongshore gradient in the mean water level close to the shoreline, the alongshore flow direction may reverse and be directed towards the centreline of the barrier leading to a converging current circulation system that cause shoreline accretion (Fig. 2).

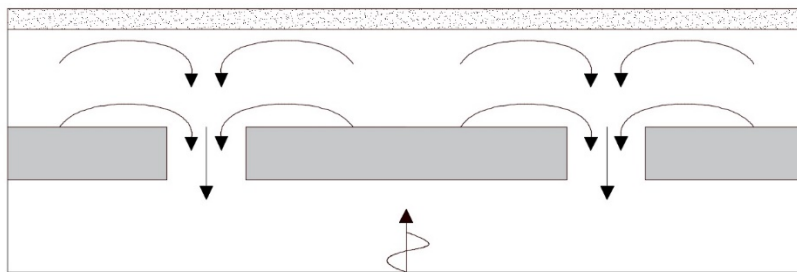


Fig. 1: Erosive circulation pattern

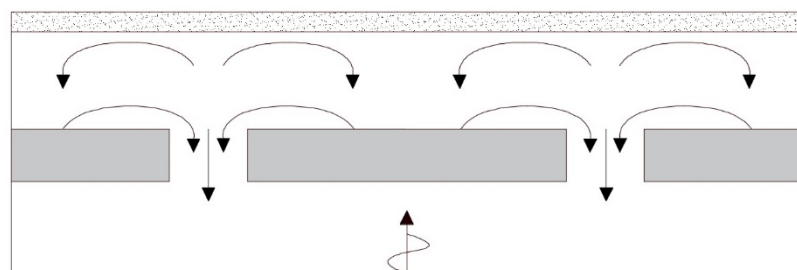


Fig. 2: Accretive circulation pattern

A plan view and a cross section of the wave basin used to perform the test is illustrated in Fig. 3. The basin is

characterized by a length equal to 17.2 m and width equal to 18.2 m. The beach has an initial steep slope (1:5) followed

by a milder slope (1:30).

There are three submerged breakwaters: the two lateral ones are 3.66 m long, and the central one is 7.32 m. The distance between the submerged breakwaters is 1.82 m.

The seaward edges of the bar sections are located at approximately  $x = 11.1$  m with the bar crest at  $x = 12$  m and their shoreward edges at  $x = 12.3$  m.

Thanks to the equations [23] it was possible to obtain the

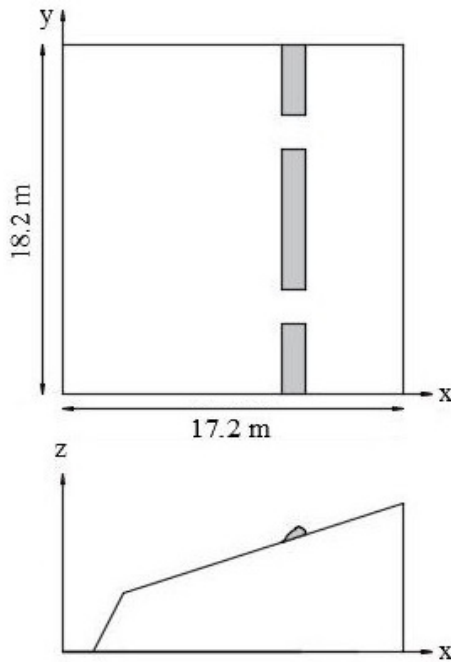


Fig.3: Plan view and cross section of the basin

dimensions of the hump considered as composed of two branches of a parabola.

In order to study the influence of rip channels and submerged breakwaters on the nearshore dynamics, the test cases B and D, with incident and monochromatic waves, have been selected (Table I). The computational grid resolution is  $\Delta x = 0.025$  m,  $\Delta y = 0.05$  m and the time step is 0.025 s

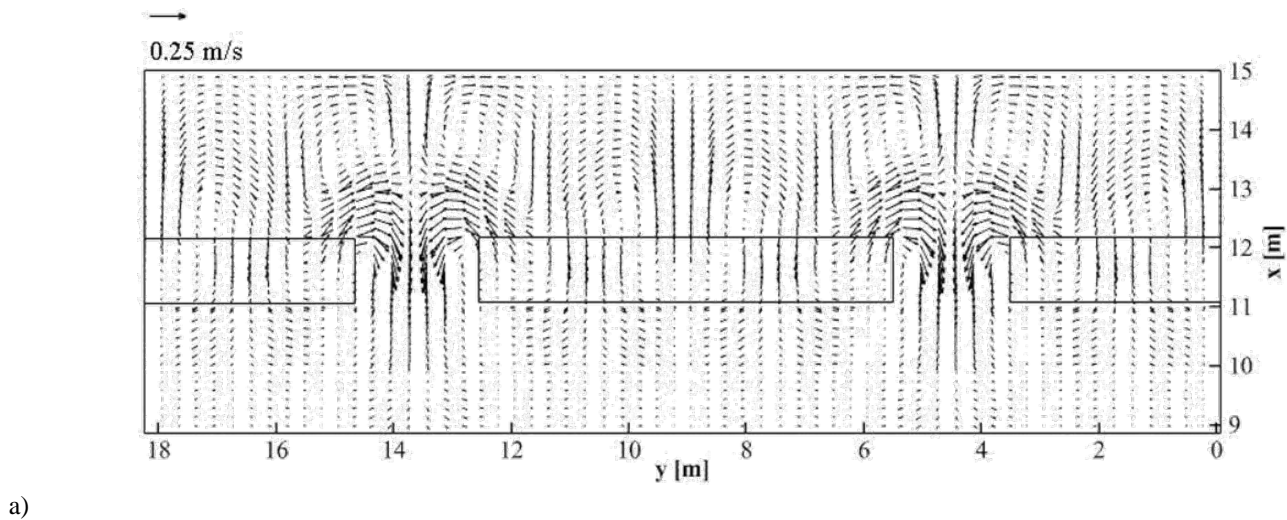
Table 1: Test conditions. Deepwater wave height  $H_0$ , wave period  $T$ , average water depth at the bar crest  $h_c$  and cross-shore location of the still water line  $x_{SWL}$

Test	$H_0$ [cm]	$T$ [s]	$h_c$ [cm]	$x_{SWL}$ [cm]
B	5.12	1	4.73	1490
D	8.26	1	2.67	1430

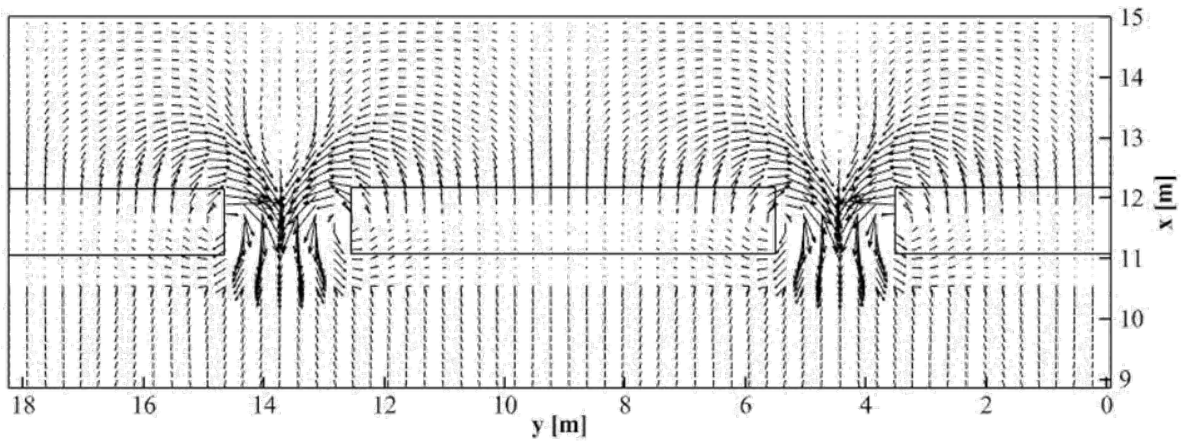
In Figure 4(a) and 4(b) the resulting plane view of the time-averaged velocity fields are shown respectively for test B and test D.

From a comparison with the above-mentioned circulation patterns (Figs. 1-2), the numerical model results clearly show an accretive mode of response for test B and an erosive mode of response for test D, in agreement with [16].

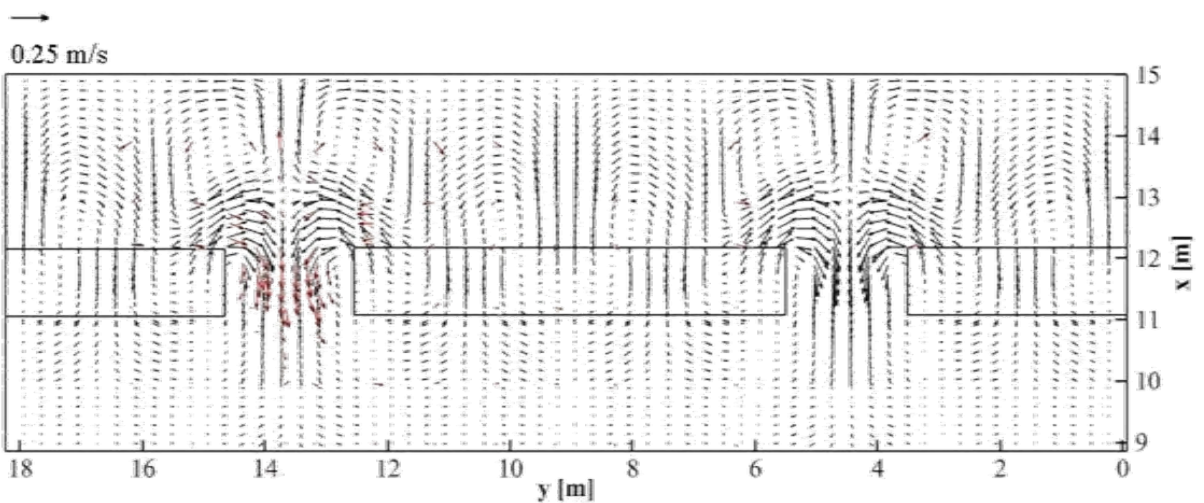
Fig. 5 shows the comparison between the resulting time-averaged velocity field for test B (a) and test D (b), and the experimental results obtained by [24]. The numerical results are in good agreement with the experimental data both in the gap between the bars and in the region area between the submerged breakwaters and the coastline.



a)



b)  
 Fig.4: Time-averaged velocity fields for (a) test B and (b) test D. A vector out of three is represented



a)  
 b)  
 Fig. 5: Time-averaged velocity fields for (a) test B and (b) test D. Comparison between the numerical results (black arrows) and the experimental measurements (red arrows – Test B) / (brown arrows – Test D) obtained by [24]

A more detailed current comparison has been analysed for two different longshore sections: the first placed in

correspondence of the onshore side of the bar, at  $x = 12.2\text{m}$  (Figs. 6a and 6b); the second placed between the bar and the shoreline, at  $x = 13.0\text{m}$  (Figs. 6c and 6d).

Fig. 6 shows the comparison between the cross-shore (U1) and longshore (U2) time-average velocity components

different longshore sections. A very good agreement observed at the two sections for both the cross-shore and longshore currents shows the ability of the numerical model to simulate the current variations.

obtained by the proposed numerical model and the laboratory data relative to test B in [15] and [25], at the two

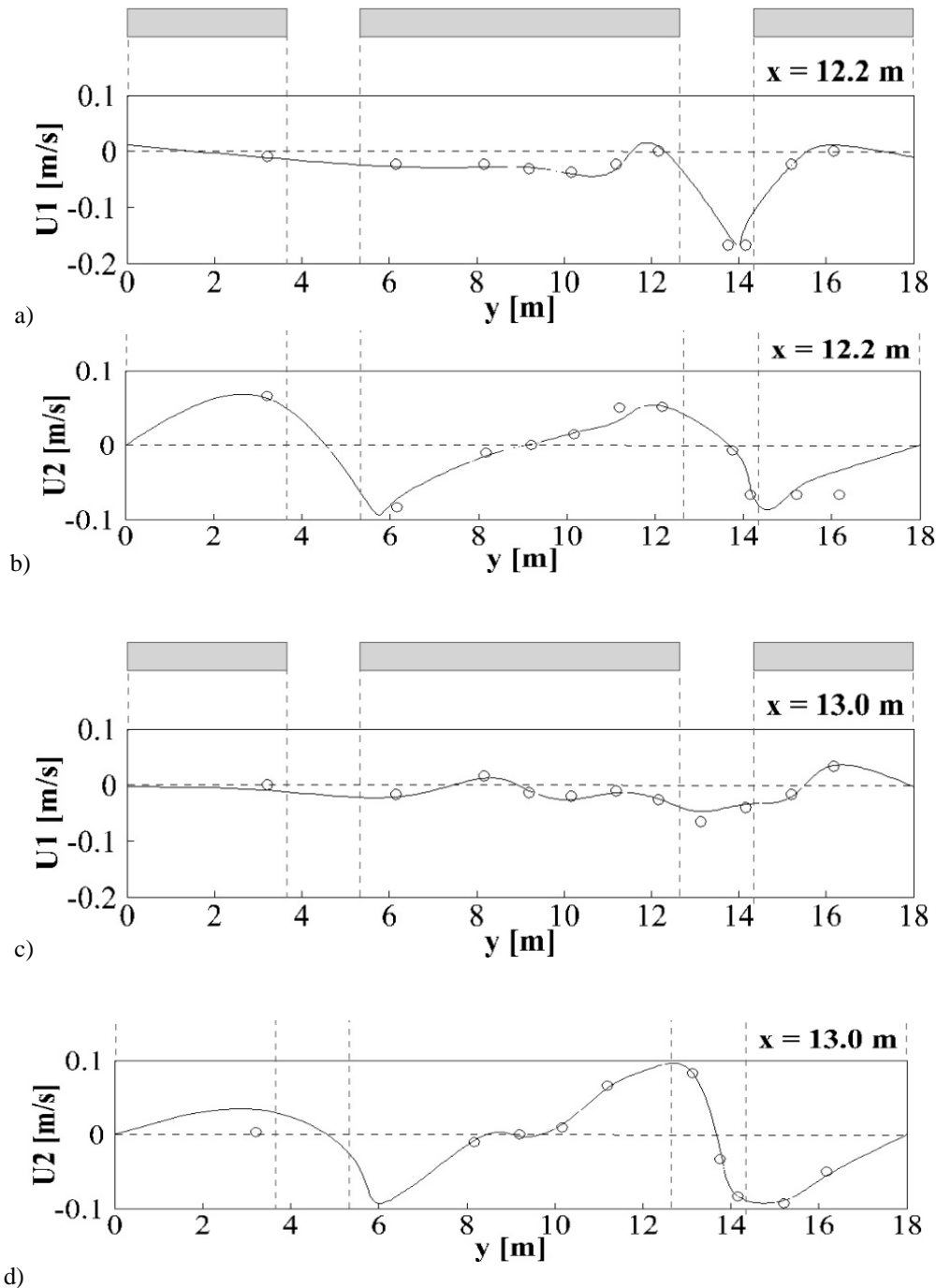


Fig.6: Cross-shore (U1) and longshore (U2) time-averaged currents for test B. Comparison between the numerical results (solid line) and the experimental measurements (circles) obtained by [12] at x =12.2 m (a;b) ; x =13 m (c;d)

Fig. 7 shows the comparison between the computed time-averaged cross-shore velocity and the experimental measurements, relative to three different longshore sections

within the gap, located respectively at: 11.5 m, x =11.8 m and x =12 m.

The cross-shore current is offshore directed in the whole gap and reaches its maximum value in the central section. The

cross-shore current is offshore directed in the whole gap and reaches its maximum value in the central section. As can be noticed from Fig. 7, the proposed

numerical model is able to simulate the current variations in fairly good agreement with the experimental measurements.

Fig. 7 shows a small underestimation of the simulated rip

current in comparison with the experimental measurements. As underlined in [9], the rip current tends to become a surface current as it flows offshore and, consequently, in this case the small differences between numerical and experimental results could be likely due to the choice of the measurement points in the water column.

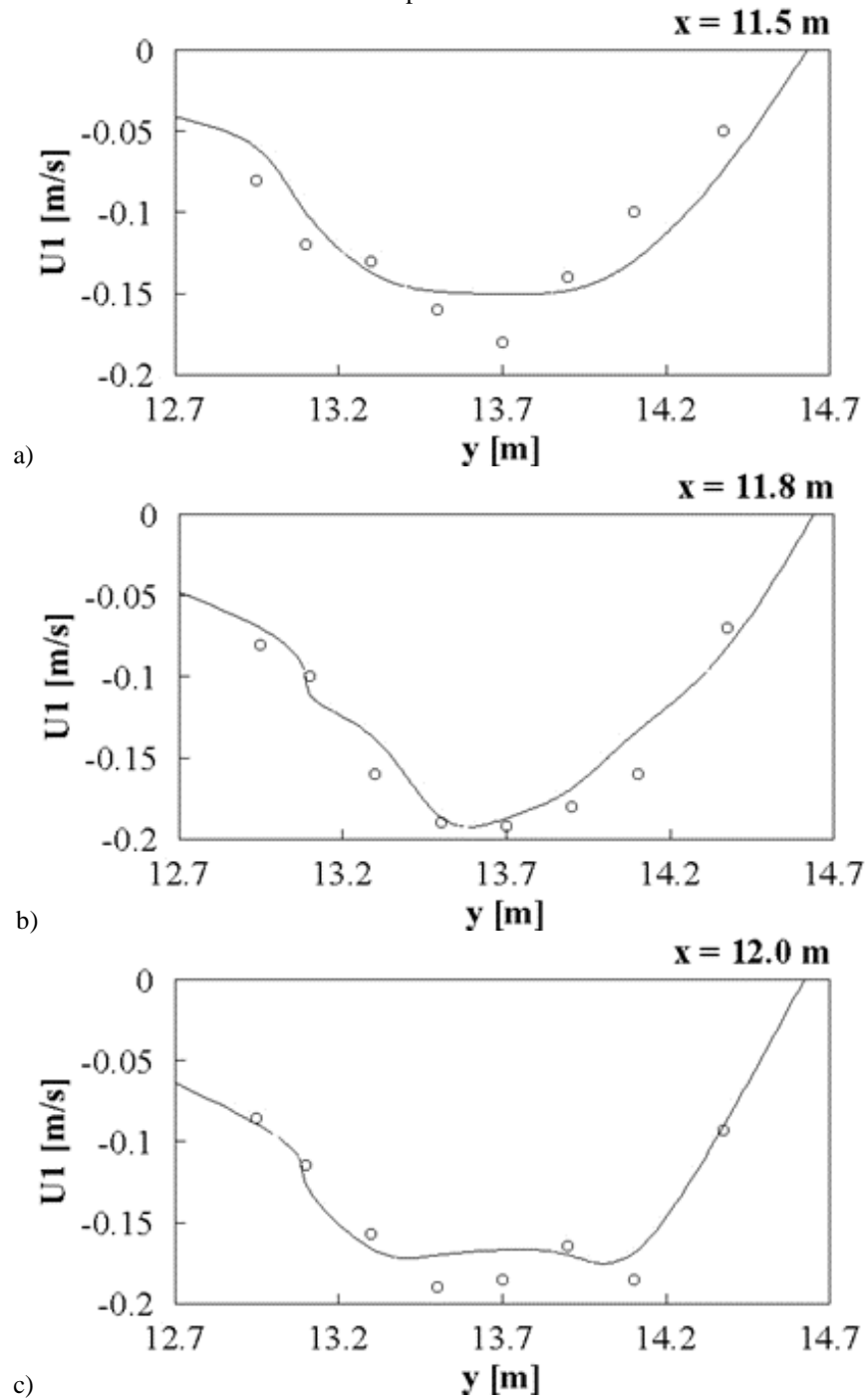


Fig.7: Cross-shore ( $U_1$ ) time-averaged currents for test B. Comparison between the numerical results (solid line) and the experimental measurements (circles) obtained by [15] in the channel at  $x=11.5 \text{ m}$  (a),  $x=11.8 \text{ m}$  (b) and  $x=12 \text{ m}$  (c)

### B. Three-dimensional structure of the circulation currents

As shown in this section, for this test case, the proposed model is able to well reproduce the three-dimensional

structure of the circulation currents by adopting only eight layers along the water depth.

The hydrodynamic phenomena produced by the wave-structure interaction have features of three-dimensionality that are locally important [9].

The most important of the above three-dimensional phenomena – which is the cause of offshore sediment transport – is the undertow [8], which consists of a circulation in the vertical plane in which the near-bed current velocities are off-shore directed in the surf zone.

Here, the vertical velocity profiles of test B obtained by means of the presented three-dimensional model are validated against the laboratory measurement of [9].

Fig. 8 shows the comparison between the vertical distribution of time-averaged cross-shore velocity obtained by the three-dimensional numerical model and

the experimental measurements presented in [9] at a location 2 m offshore of the bar ( $x = 9.0$  m,  $y = 13.6$  m) and a location inside the channel ( $x = 11.75$  m,  $y = 13.6$  m).

The results are normalized by the celerity  $c = \sqrt{Gh}$  where  $G$  is the constant of gravity and  $h$  is the depth of still water.

From Fig. 8, it can be seen that the vertical velocity exhibit strong depth variations, twisting over depth, with the surface velocity going mainly offshore and the bottom current going shoreward.

In particular, at the offshore location ( $x = 9.0$  m,  $y = 13.6$  m) the largest (offshore directed) current is located at the free surface, whereas the weakest (onshore directed) current is near the bottom.

Inside the channel ( $x = 11.75$  m,  $y = 13.6$  m) the cross-shore current shows higher magnitude and a maximum value at mid-depth.

The good agreement between numerical results and experimental measurements shows the ability of the model to simulate the variations of the velocity field along the vertical direction.

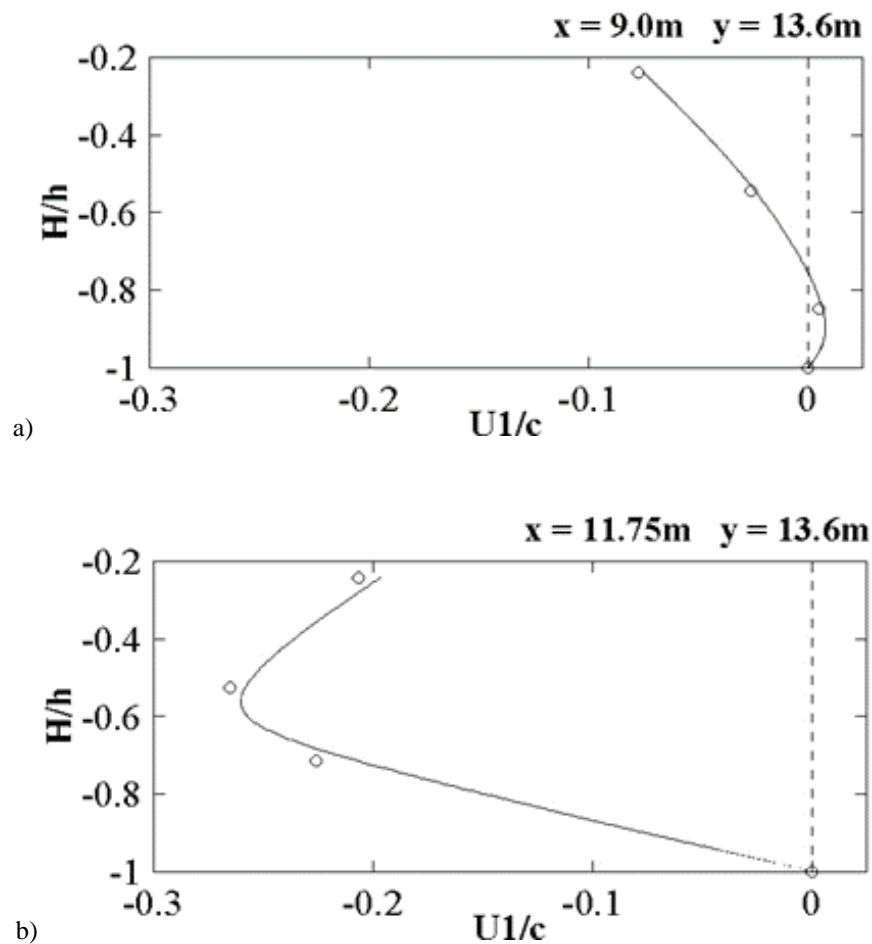


Fig.8: Vertical distribution of cross-shore time-averaged current for test B. Comparison between the numerical results (solid line) and the experimental measurements (circles) obtained by [9] at points:  $x = 9.0$  m,  $y = 13.6$  m (a) and  $x = 11.75$  m,  $y = 13.6$  m (b)

In Fig. 9 two different cross-shore sections are show,

respectively at  $y=8.45\text{m}$  and  $y=9.20\text{m}$  where the undertow is visible. The undertow represents a mass conservation response to the associated landward drift of water under the crests of the breaking incident waves. That's because, physically, nearshore, the wave induced mass flux between wave crest and trough is onshore directed. These currents are the main cause of cross-

shore transport of suspended sediment picked-up by the wave-breaking-induced turbulence. As can be observed in Fig. 9, the vertical structure of the mean horizontal flow under breaking waves is characterized by onshore directed velocities near the free surface and offshore directed velocities near the bottom (undertow). In both sections the current is stronger on the landward side of the submerged breakwaters, where the waves break.

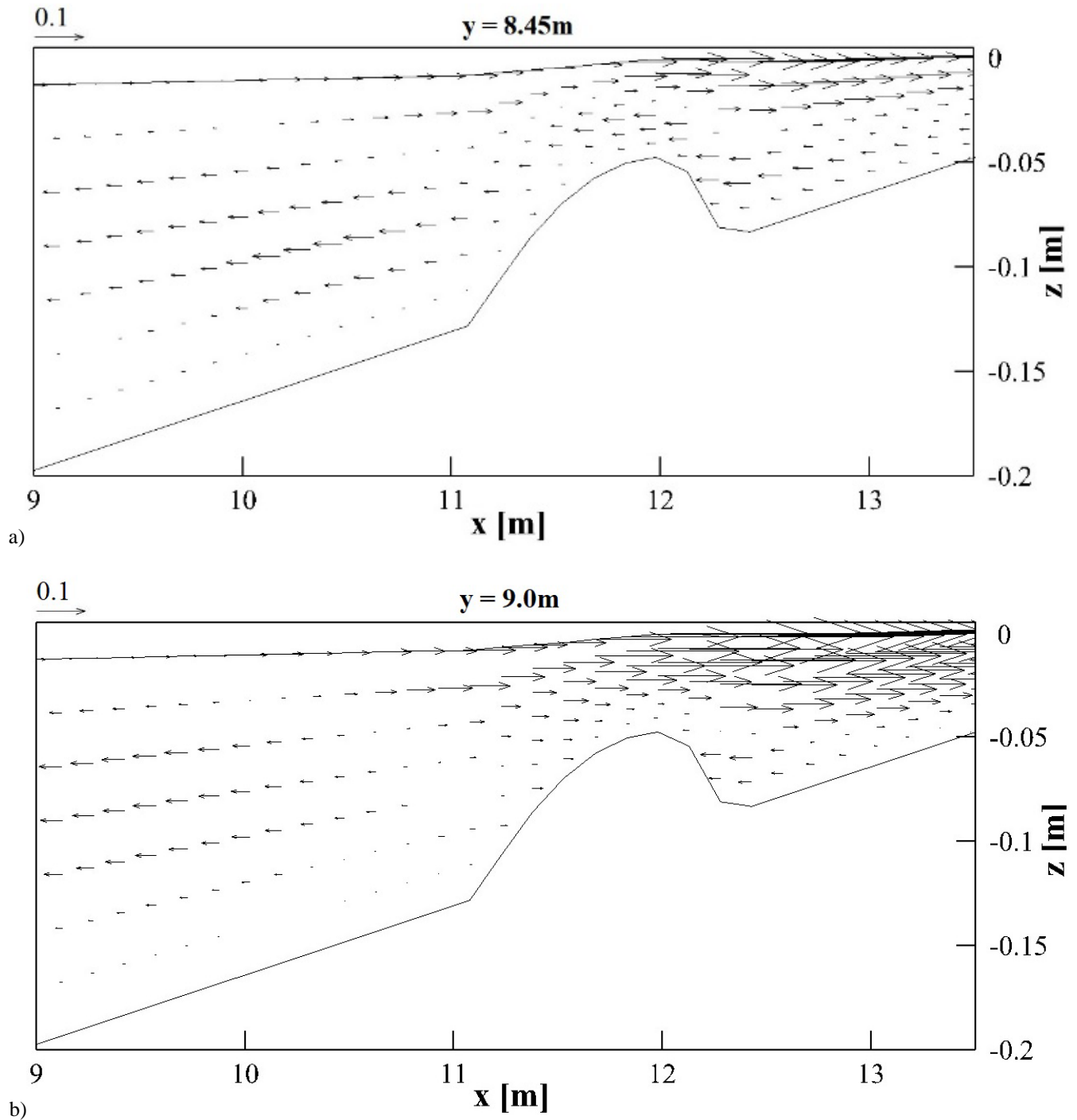


Fig.9: Cross-shore time-averaged currents for test B obtained by three-dimensional numerical model at: a)  $y = 8.45\text{ m}$  and b)  $y=9.0\text{ m}$

In order to show that the accuracy of the results is improved by running the model in its three-dimensional version, a comparison – in terms of vertical time-averaged cross-shore velocity – with the two-dimensional depth-averaged model presented in [11] is shown in Fig. 10.

From the Figure, it is evident that the three-dimensional and two-dimensional depth-averaged values do not give informations about the undertow phenomenon, that is correctly represented by the results obtained by three-dimensional model.

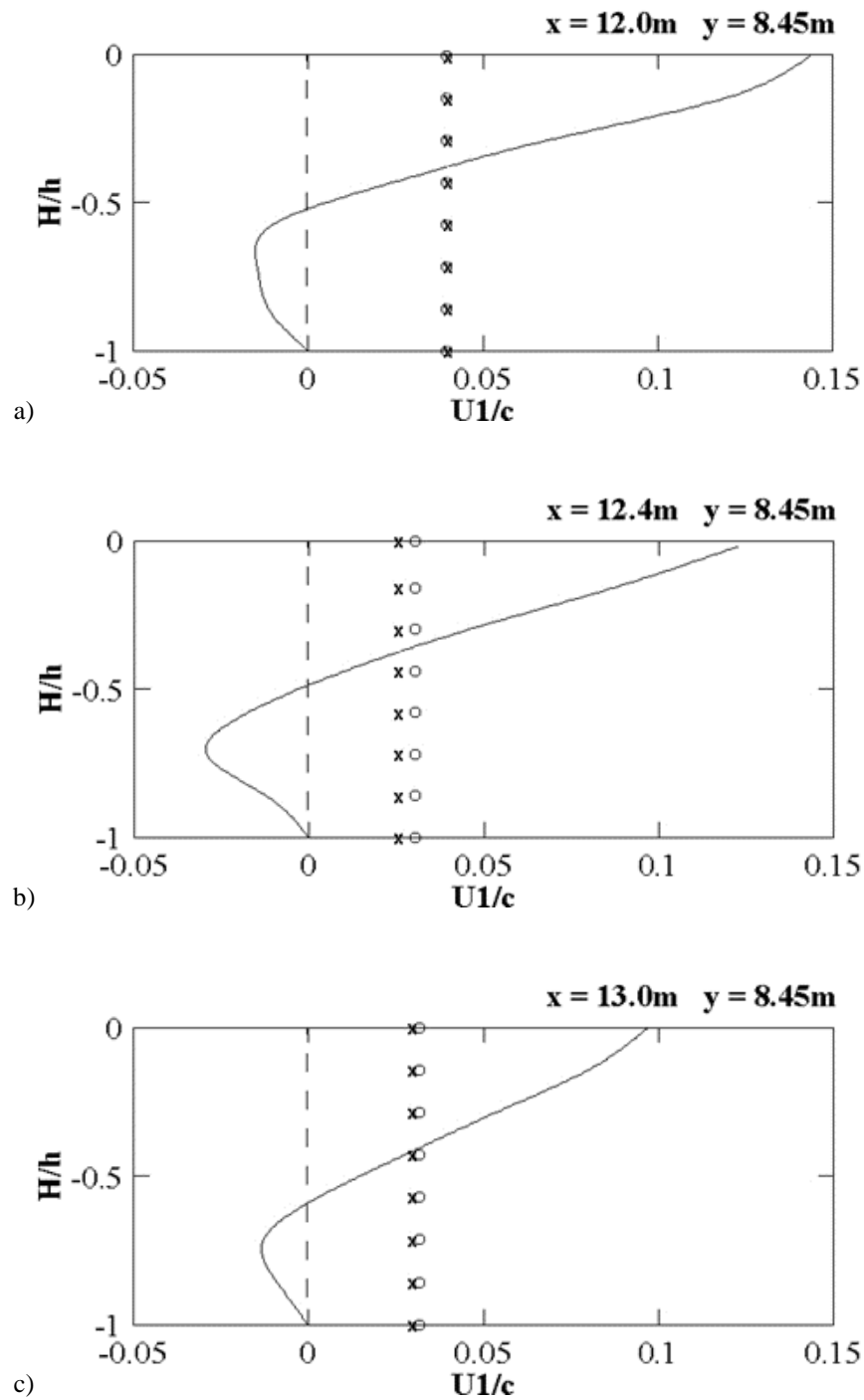


Fig.10: Vertical time-averaged cross-shore velocity profile for test B. Comparison between the three-dimensional numerical results (solid line), depth-averaged three-dimensional numerical results (crosses) and the two-dimensional depth-averaged numerical results obtained with the [11] model (circles) at points: a)  $x = 12.0\text{m}$   $y = 8.45\text{m}$ , b)  $x = 12.4\text{ m}$   $y = 8.45\text{ m}$  and c)  $x = 13.0\text{ m}$   $y = 8.45\text{ m}$

## IV. CONCLUSION

A three-dimensional non-hydrostatic model for free-surface flow simulations, based on an integral form of the Navier-Stokes equations in a time-dependent coordinate system, has been proposed. The proposed model has been used to simulate the free-surface elevation and velocity fields induced by the interaction between incident waves and submerged breakwaters. The numerical results have

been compared with experimental data [15]-[9] and with results obtained by a depth averaged horizontal two-dimensional model [11].

The comparison between the numerical results and the experimental measurements shows the ability of the proposed model to simulate the three-dimensional velocity fields induced by the wave-structure interaction.

The comparison between the numerical results obtained by the depth-averaged two-dimensional model and those obtained by the proposed three-dimensional model shows that only the latter can correctly simulate the undertow, which consists of a circulation in the vertical plane in which the current velocities are onshore directed near the free-surface and offshore directed near the bed.

## REFERENCES

- [1] G. Querzoli, S. Fortini, S. Espa, M. Costantini, and F. Sorgini, "Fluid dynamics of aortic root dilation in Marfan syndrome", *Journal of Biomechanics*, vol. 47, 2014, pp. 3120-3128.
- [2] A. Pellicioni, P. Monti, and G. Leuzzi, "Wind-speed profile and roughness sublayer depth modelling in urban boundary layers", *Boundary-Layer Meteorology*, vol. 160, 2016, pp. 225-248.
- [3] A. Di Bernardino, P. Monti, G. Leuzzi, G. Querzoli, "Water-channel estimation of Eulerian and Lagrangian time scale of the turbulence in idealized two-dimensional urban canopies", *Boundary-Layer Meteorology*, vol. 165, pp. 251-276.
- [4] G. Cannata, L. Barsi, and F. Gallerano, "Numerical investigation of the coupled flutter onset mechanism for streamlined bridge deck cross-sections", *WSEAS Transactions on Fluids Mechanics*, vol. 12, 2017, pp. 43-52.
- [5] G. Cannata, L. Barsi, and F. Gallerano, "Numerical simulation of the coupled flutter instability for closed-box bridge decks", *International Journal of Mechanics*, vol. 11, 2017, pp. 128-140.
- [6] R. Ranasinghe, M. Larson, and J. Savioli, "Shoreline response to a single shore-parallel submerged breakwaters", *Coastal Engineering*, vol. 57, 2010, pp. 1006-1017.
- [7] G. Cannata, C. Petrelli, L. Barsi, and F. Gallerano, "3D Free Surface Flow Simulations Based on the Integral Form of the Equations of Motion", *WSEAS Transactions on Fluids Mechanics*, vol.12, 2017, pp. 166-175.
- [8] R. Deigaard, P. Justesen, and J. Fredsøe, "Modelling undertow by a one-equation turbulence model", *Coastal Engineering*, vol. 15, 1991, pp. 431-458.
- [9] K. A. Haas, and Ib. A. Svendsen, "Laboratory measurements of the vertical structure of a rip current", *Journal of Geophysical Research*, vol. 107, 2002, pp. 15-1-15-19.
- [10] F. Gallerano, G. Cannata, O. De Gaudenzi, and S. Scarpone, "Modeling Bed Evolution Using Weakly Coupled Phase-Resolving Wave Model and Wave-Averaged Sediment Transport Model" *Coastal Engineering Journal*, vol. 58, 2016, pp. 1-50.
- [11] F. Gallerano, G. Cannata, and F. Lasaponara, "A new numerical model for simulations of wave transformation, breaking and long-shore currents in complex coastal regions", *International Journal for Numerical Methods in Fluids*, vol.80, 2016, pp. 571-613.
- [12] G. Cannata, L. Barsi, C. Petrelli, and F. Gallerano, "Numerical investigation of wave fields and currents in a coastal engineering case study", *WSEAS Transactions on Fluids Mechanics*, vol. 13, 2018, pp. 87-94.
- [13] Q. Chen, R. A. Dalrymple, J. T. Kirby, A. B. Kennedy, and M. C. Haller, "Boussinesq modeling of a rip current system", *Journal of Geophysical Research*, vol. 104, 1999, pp. 20,617-20,637.
- [14] F. Gallerano, G. Cannata, F. Lasaponara, and C. Petrelli, "A new three-dimensional finite-volume non-hydrostatic shock-capturing model for free surface flow", *Journal of Hydrodynamics*, vol. 29, 2017, pp. 552-566.
- [15] M. C. Haller, R. A. Dalrymple, and Ib. Svendsen, "Experimental study of nearshore dynamics on a barred beach with rip channels", *Journal of Geophysical Research*, vol. 107, 2002, pp. 14-1-14-21.
- [16] M. Villani, J. Bosboom, M. Zijlema, and M.J.F. Stive, "CIRCULATION PATTERNS AND SHORELINE RESPONSE INDUCED BY SUBMERGED BREAKWAERS", *Paper presented at the Proceedings of the 33<sup>rd</sup> International Conference on Coastal Engineering, Santander*, 2012.
- [17] R.J. Spiteri, and S.J. Ruuth, "A new class of optimal high-order strong-stability preserving time discretization methods", *SIAM Journal on Numerical Analysis*, vol. 40, 2002, pp. 469-491.
- [18] M. Rosenfeld, and D. Kwak, "Time-dependent solutions of viscous flows in moving co-ordinates", *International Journal for Numerical Methods in Fluids*, vol. 13, 1991, pp. 1311-1328.
- [19] U. Trottenberg, C.W. Oosterlee, and A. Schuller, "Multigrid Academic Press," NY
- [20] G. Cannata, F. Lasaponara, and F. Gallerano, "Non-linear Shallow Water Equations numerical integration on curvilinear boundary-conforming grids", *WSEAS Transactions on Fluids Mechanics*, vol. 10, 2015, pp. 166-175.
- [21] G. Cannata, C. Petrelli, L. Barsi, F. Fratello, and F. Gallerano, "A dam-break flood simulation model in curvilinear coordinates", *WSEAS Transactions on Fluids Mechanics*, vol. 13, 2018, pp.60-70.
- [22] A. Harten, P. D. Lax, and B. Van Leer, "On Upstream Difference and Godunov-Type Schemes for Hyperbolic Conservation Laws", *SIAM Review*, vol. 25, 1983, pp. 35-61.
- [23] G. Bellotti, "A simplified model of rip currents systems around discontinuous barriers", *Coastal Engineering*, vol. 51, 2004, pp. 323-335.
- [24] M.C. Haller, R.A. Dalrymple, and Ib.A. Svendsen, "Experimental Modeling of a Rip Current System," *Proceedings of the Third International Symposium on Ocean Wave Measurement and Analysis, Virginia Beach, VA, USA, 1997b*, pp. 750-746.
- [25] K.A. Haas, Ib.A. Svendsen, M.C. Haller, and Q. Zhao, "Quasi-three-dimensional modelling of rip current systems", *Journal of Geophysical Research*, vol. 108, 2003, pp. 10-21.